PHYSICAL REVIEW A **67**, 012502 (2003)

Linear dichroism of the 4*f* photoemission in the giant resonance of atomic europium

J. Schulz,* Ph. Wernet,† M. Martins, and B. Sonntag
Institut für Experimentalphysik, Luruper Chaussee 149, 22761 Hamburg, Germany

R. Müller, K. Godehusen,‡ and P. Zimmermann
Institut für atomare Physik und Fachdidaktik, Hardenbergstrasse 36, 10629 Berlin, Germany

(Received 23 August 2002; published 21 January 2003)

The linear dichroism in the 4f photoelectron spectra of atomic Eu excited at photon energies in the range of the giant 4d-4f resonance have been determined. Dramatic changes of the dichroism have been observed when tuning the photon energy through the giant resonance. The dichroism patterns are compared to the predictions of a model based on *LS* coupling which takes the interaction of the discrete resonances with the ionization continua into account.

DOI: 10.1103/PhysRevA.67.012502 PACS number(s): 33.60.Cv, 32.80.Fb

I. INTRODUCTION

Dichroism in the photoemission of rare earths and rare earth compounds is a powerful tool for probing the magnetic structure of surfaces and thin films ([1,2], and references therein). Gadolinum (Gd) with its half filled 4f shell plays a key role in these studies. The Gd 4f-shell is well localized in the solid state explaining the good agreement of the spectra with the predictions of ionic models [3–6]. The atomic approach is further supported by the close similarities of the dichroism in the 4f and 4d photoelectron spectra of atomic europium and of thin gadolinium films [7,8]. The typical dichroism patterns [9] could be verified in all photoelectron spectra when the fine-structure components of the 4f and 4d multiplets were resolved. In agreement with the theoretical predictions the dichroism in the nonresonant 4f photoelectron spectra of atomic Eu vanishes when integrated over all fine structure components of the 4f multiplet. For photon energies close to atomic resonances this sum rule is expected to break down. The dichroism observed in the photoabsorption of solid Gd in the photon-energy range of the giant 4d-4f resonance is a clear evidence for this breakdown [10].

In order to get a deeper understanding for this effect we studied the linear alignment dichroism (LAD) and the linear magnetic dichroism (LMDAD) in the Eu 4f photoelectron spectra excited by photons in the energy range of the giant resonance. The experimental results are compared to the predictions of a model based on Fanos description of atomic resonances [11] and the description of the angular distribution of photoelectrons within *LS* coupling [12]. Our theoretical approach is similar to the model by Starke and coworkers [13] describing the magnetic circular dichroism in the photoelectron spectra of solid Gd excited in the giant resonance, but the Fano-type energy dependence of the dipole matrix elements has been included explicitly and the theory of the angular distribution of photoelectrons [12] has been used in order to extend the theory to linear dichroism in the angular distribution. A similar model calculating the angular distributions of photoelectrons within a resonance has been published [24].

II. EXPERIMENTAL SETUP

A thermal atomic europium beam was produced by a resistively heated oven. The atoms were ionized using linearly polarized undulator radiation monochromatized by a SX700 monochromator at the BW3 beamline of the DORIS storage ring in Hamburg (Germany). The 4f photoelectrons were detected with a scienta SES200 electron analyzer set at the magic angle with respect to the electric-field vector of the undulator radiation. The individual bandwidths of the spectra are given in the figure captions. All bandwidths have been determined by fitting Gaussian lines to the spectra and by rare-gas calibration measurements. For unpolarized atoms the photoelectron spectra are proportional to the total 4f photoionization cross section. The Eu atoms were aligned (oriented) by optical pumping with a linearly (circularly) polarized laser beam tuned to the $4f^7\,6s^2\;{}^8S_{7/2}\rightarrow 4f^7\,6s\,6p\;{}^8P_{5/2}$ transition at a wavelength of 466.2 nm. The laser beam propagated antiparallel to the ionizing synchrotron radiation. For a more detailed description of the experimental setup see Refs. [8,14].

III. HIGH-RESOLUTION 4*f* PHOTOELECTRON SPECTRUM

It is well established that final-state configuration interactions can influence the photoelectron spectra of the rare-earth metals significantly [15,16]. In the Eu 4f photoionization the $4f^6\,6s^2\;{}^7F_{0\dots6}$ final states strongly overlap with states of the configurations $4f^6\,5d\,5s$ and $4f^6\,5d^2$. This leads to a complicated Eu 4f photoelectron spectrum displaying more than the seven lines predicted by the *LS*-coupling model [17].

Figure 1 shows the Eu 4f photoelectron spectrum taken at a photon energy of 49 eV. This spectrum corroborates the spectrum presented in Ref. [17] but reveals additional lines

---

*Electronic address: Joachim.Schulz@maxlab.lu.se; present address: MAX-lab, Box 118, 221 00 Lund, Sweden.

†Present address: SSRL, 2575 Sand Hill Road, MS 69, Menlo Park CA 94025.

‡Present address: BESSY GmbH, Albert-Einstein-Strasse 15, 12489 Berlin, Germany.

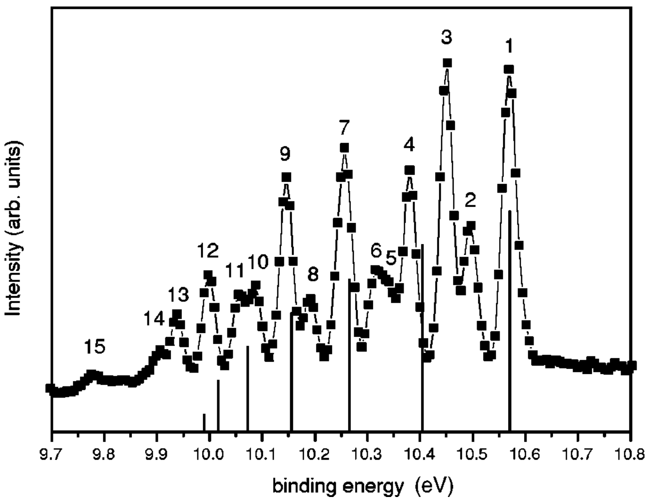

FIG. 1. Eu $4f$ photoelectron spectrum taken at a photon energy of 49 eV. The experimental resolution has been determined to 33 meV. To guide the eyes the data points have been connected by a solid line. The solid bar spectrum shows the pure Eu $4f^6\,6s^2\;{}^7F_{0\ldots6}$ multiplet as expected in pure *LS* coupling.

that have been not resolved. The bar spectrum of Fig. 1 gives the predictions for the Eu $4f^6\,6s^2\;{}^7F_{J_f}$ multiplet obtained by a pure *LS*-coupling model. The relative intensities are given by the multiplicity of the final ionic state $(2J_f+1)$ and the relative positions are given by Landés interval rule. The ${}^7F_6$ line has been matched to the position of line 1. While the lines 1, 7, and 9 can be clearly assigned to the final states${}^7F_6$, ${}^7F_4$, and ${}^7F_3$ a straightforward assignment of the other lines is not possible. In the vicinity of the predicted energy position for the ${}^7F_5$ state two prominent lines (No. 3 and 4) have been measured. This is a clear indication for a strong interaction of the ${}^7F_5$ state with additional states of the same total angular momentum $J_f=5$.

To shed light onto the possible configuration interactions in Table I the experimental binding energies are compared to Eu II energy levels obtained by optical spectroscopy [18]. The first three columns give the numbers of the 15 lines in Fig. 1 together with their assignments and binding energies. The very tentative assignments of the ${}^7F_{J_f}$ states with $J_f=5$, 2, 1, and 0 are set in parentheses. The energy calibration has been done in respect to the first Eu $4f^7\,6s$ ionization thresholds. The absolute uncertainties of the binding energies amount to 20 meV. The three columns on the right-hand side of Table I show Eu II energy levels derived from spark spectra together with their total angular momenta *J*. Where an assignment is given in the reference it is included in the last column. The comparison does not allow for an identification of all the lines but it can be clearly seen that many lines coincide within the experimental uncertainties with unassigned energy levels from Ref. [18] carrying the matching angular momentum.

Table I demonstrates that states of the Eu $4f^6\,5d^2\;{}^7P_{2,3,4}$ and the $4f^6\,5d^2\;{}^9P_{3,4,5}$ multiplets coincide in energy with the high binding-energy states of the $4f^6\,6s^2\;{}^7F_{0\ldots6}$ multiplet. In particular the $4f^6\,5d^2\;{}^9P_5$ line nearly coincides with the lines No. 4 and 5 in Fig. 1. Mixing of this state with the $4f^6\,6s^2\;{}^7F_5$ state provides a possible explanation for the occurrence of two intense lines close to the energy where the *LS*-coupling model predicts the $4f^6\,6s^2\;{}^7F_5$ line.

TABLE I. Assignment and binding energies (in eV) of the lines observed in the Eu $4f$ photoelectron spectrum presented in Fig. 1 compared to Eu II energy levels published in Ref. [18].

This work			Optical data [18]		
No.	Assignment	E_B ± 0.02	E_B	J	Assignment
1	${}^7F_6$	10.57	10.58	6	
			10.52	4	$4f^6({}^7F)5d^2\;{}^7P_4$
2		10.50	10.48	3	$4f^6({}^7F)5d^2\;{}^7P_3$
			10.48	5	
3		10.45	10.47	7	
4	$({}^7F_5)$	10.38	10.37	5	
5		10.34	10.36	5	$4f^6({}^7F)5d^2\;{}^9P_5$
6		10.31	10.30	2	$4f^6({}^7F)5d^2\;{}^7P_2$
			10.29	4	$4f^6({}^7F)5d^2\;{}^9P_4$
7	${}^7F_4$	10.26	10.25	4	
			10.21	3	$4f^6({}^7F)5d^2\;{}^9P_3$
			10.21	5	$4f^6({}^7F)5d\,6s\;{}^9P_5$
8		10.19	10.19	4	
9	${}^7F_3$	10.15	10.13	4	
10		10.09	10.08	3	
11	$({}^7F_2)$	10.06	10.08	4	$4f^6({}^7F)5d\,6s\;{}^9P_4$
12	$({}^7F_1)$	10.00			
13	$({}^7F_0)$	9.94	9.93	3	$4f^6({}^7F)5d\,6s\;{}^9P_3$
14		9.90	9.88	3	
14			9.88	2	
15		9.78			

In conclusion of this section it can be said that details of the fine structure of the Eu $4f$ photoelectron spectrum cannot be explained by a single configuration model. Inspite of this, studies of the linear dichroism in the nonresonant photoelectron spectra of this multiplet demonstrated that the characteristic dichroism patterns can be explained by models based on the *LS*-coupling scheme [7,9,17]. Keeping this in mind we will develop an *LS*-coupling model for explaining the linear dichroism in the angular-resolved photoelectron spectra excited within the giant Eu $4d$ resonance in the subsequent sections. This model will provide a qualitative explanation for the variations of the patterns when tuning the photon energy through the resonance.

IV. ENERGY-INTEGRATED $4f$ PHOTOELECTRON SPECTRA

Figure 2 shows the Eu $4f$ photoionization cross section for unpolarized Eu atoms obtained by integrating over the components of the $4f^6\;{}^7F$ photoelectron multiplet. The data have been taken in two different runs. In the run represented by squares the photon energy was first scanned in steps towards higher energies and then the direction of the scan was reversed. The run represented by circles has been taken in a single run. The drift of the atomic beam source is mainly

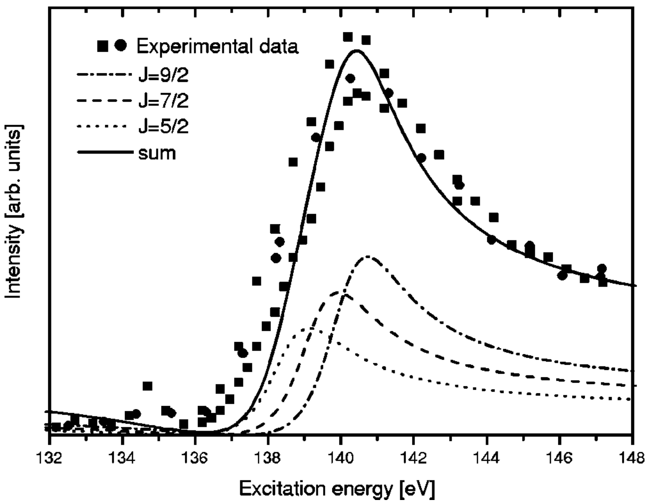

FIG. 2. Eu $4f$ photoionization cross section in the energy range of the giant $4d$-$4f$ resonance (circles and squares). The data have been obtained in two different runs. The solid curve represents the sum of the three partial cross sections $4f^7\,6s^2\;{}^8S_{7/2}\rightarrow 4f^6\,6s^2\epsilon l\;{}^8P_J$ with $J=5/2$ (dotted curve), 7/2 (dashed curve), 9/2 (dash dot). The monochromator bandwidth has been determined to less than 150 meV.

responsible for the scatter of the experimental data points.

In the following we will focus on the prominent asymmetric resonance peaking at 140.3 eV and neglect the smaller structures at the threshold. The giant resonance is dominated by the transitions $4d^{10}\,4f^7\,6s^2\;{}^8S_{7/2}\rightarrow 4d^9\,4f^8\,6s^2\;{}^8P_J$ with $J=5/2,7/2,9/2$. These states mainly autoionize into the $(4d^{10}4f^6\;{}^7F_{J_f}+\epsilon l)^8P_J$ continua with $J=5/2,7/2,9/2$, $J_f=0\cdots 6$ and $l=2,4$ [19,20]. In this approximation J conservation results in three independent discrete states each coupled to a separate set of ionization continua. These three independent resonances can be described using the Fano-type model explained in Sec. V.

In Fig. 2 the Fano profiles for the $(4d^{10}\,4f^6\;{}^7F_{J_f}+\epsilon l)^8P_J(J=5/2,7/2,9/2)$ partial cross sections are included. In agreement with the results of Hartree-Fock calculations and the results presented by Moewes *et al.* [20] the energy positions of the resonances are separated by 0.8 eV. The resonance energies increase with increasing total angular momentum J. The same holds for the partial cross section because they have been set proportional to their statistical weight $(2J+1)$. Summing this partial cross sections yields the total $4f$ ionization cross section given by the solid line. This line, within the experimental uncertainties, describes the experimental data reasonably well. The marked deviations on the low-energy rise are due to the neglect of intermediate states not allowed in pure LS coupling.

V. *LS*-COUPLING MODEL

The angle-resolved photoemission intensity I of polarized atoms can be described by [12]

$$I=K_{exp}\frac{\sigma}{4\pi}\sum_{k_0kk_\gamma}A_{k_00}B_{k_0kk_\gamma}F_{k_0kk_\gamma}, \tag{1}$$

where K_{exp} is an experimental constant. The multipole moments A_{k_00} denote the normalized ground-state polarization. The parameters $F_{k_0kk_\gamma}$ are geometric factors depending on the polarization directions of the atoms and the ionizing radiation and on the position of the detector. The parameters $B_{k_0kk_\gamma}$ describe the photoionization process and contain the reduced dipole transition-matrix elements

$$D_{J,l,j,J_f}=\langle L_fS_fJ_f,lj:J||D||L_0S_0J_0\rangle, \tag{2}$$

where L_0, S_0, and J_0 are the quantum numbers of the ${}^8S_{7/2}$ ground state. L_f, S_f, and J_f are the quantum numbers of the final ionic states that are limited to purely LS-coupled ${}^7F_{0\ldots 6}$ states. l and j are the quantum numbers of the emitted electron. The total angular momenta of the final ionic state and the emitted electron are coupled to the final-state angular momentum $J=5/2,7/2,9/2$. The dependence of the matrix elements on the total angular momentum of the electron j and of the final ionic state J_f can be eliminated by recoupling the final state into LS-coupled terms:

$$|L_fS_fJ_f,lj:J\rangle=\sum_{LS}\hat{L}\hat{S}\hat{J}_f\hat{j}\begin{Bmatrix} L_f & l & L\\ S_f & \frac{1}{2} & S\\ J_f & j & J\end{Bmatrix}\times\left|L_fl[L]S_f\frac{1}{2}[S]:J\right\rangle \tag{3}$$

using the notation $\hat{L}=(2L+1)^{1/2}$.

In a previous publication [9] dealing with linear dichroism in the nonresonant $4f$ photoemission it has been shown that the dependence of the B parameters on the final-state angular momenta J_f is solely given by the Wigner-9j symbol in Eq. (3), if the photoionization process is mainly determined by dipole transition-matrix elements

$$D^{\rm cont}_{J,l}=\langle L_fl[L]S_f\tfrac{1}{2}[S]:J||D||L_0S_0J_0\rangle, \tag{4}$$

for direct ionization, that change slowly with the photon energy.

For excitation energies near the giant resonance this condition does not hold since the same final states can be reached also via the excitation of discrete $4d^9\,4f^8\;{}^8P_J$ intermediate states described by the dipole matrix elements

$$D^{\rm disc}_{J,l}=\langle LSJ'||D||L_0S_0J_0\rangle, \tag{5}$$

and subsequent autoionization. L, S, and $J'=J$ are the quantum numbers of the intermediate state. The autoionization leads to a coupling of the discrete intermediate states with the final continuum states giving rise to nondiagonal matrix elements of the Hamilton operator,

$$V_{J,l}=\langle L_fl[L]S_f\tfrac{1}{2}[S]:J|H|LSJ'\rangle, \tag{6}$$

following the common notation for $l=2$ the index d and for $l=4$ the index g will be used.

An appropriate way to describe the interference between those different channels is given by the Fano theory. In a frequently cited paper from 1961 Fano presented a theory for calculating the interaction of a single discrete resonance with one or more continuum states [11]. In this work Fano showed that the resonant absorption can be easily described by introducing energy-dependent final states $|\Psi_{J,i,E}\rangle$ that are eigenstates of the Hamiltonian containing the interactions of the continua with the discrete state.

Since for each value of J two continuum states distinguished by $l=2$ and 4 have to be considered in the *LS*-coupling scheme, there are only two Fano states for each resonance. The energy dependence of the excitation of state $|\Psi_{J,1,E}\rangle$ is given by a Fano profile. The state $|\Psi_{J,2,E}\rangle$ is not coupled to the discrete state, and therefore the excitation is energy independent. The two Fano states can be represented in the form

$$|\Psi_{J,i,E}\rangle=a_{J,i,E}|LSJ\rangle + \int dE'\left[\sum_{l} b_{J,i,l,E,E'}\left|L_f l[L]S_f\frac{1}{2}[S]:J\right\rangle\right]. \tag{7}$$

The coefficients $a_{J,i,E}$ and $b_{J,i,l,E,E'}$ contain the matrix elements $V_{J,d}$ and $V_{J,g}$. Under the assumption that these matrix elements are nearly constant over the range of the giant resonance, the integral in Eq. (7) can be calculated and the coefficients $a_{J,i,E}$ and $b_{J,i,l,E=E'}$ are given by [21]

$$a_{J,1,E}=\frac{-|V_J|}{\sqrt{(E-E_J)^2+(\Gamma_J/2)^2}}, \tag{8a}$$

$$b_{J,1,d,E}=\frac{-V_{J,d}}{|V_J|}\,\frac{E-E_J}{\sqrt{(E-E_J)^2+(\Gamma_J/2)^2}}, \tag{8b}$$

$$b_{J,1,g,E}=\frac{-V_{J,g}}{|V_J|}\,\frac{E-E_J}{\sqrt{(E-E_J)^2+(\Gamma_J/2)^2}}, \tag{8c}$$

$$a_{J,2,E}=0, \tag{8d}$$

$$b_{J,2,d,E}=\frac{V^*_{J,g}}{|V_J|}, \tag{8e}$$

$$b_{J,2,g,E}=\frac{-V^*_{J,d}}{|V_J|}, \tag{8f}$$

with

$$|V_J|=\sqrt{|V_{J,d}|^2+|V_{J,g}|^2}. \tag{8g}$$

Taking excitation and autoionization of the $|\Psi_{J,i,E}\rangle$ states into account the reduced dipole transition-matrix elements describing the photoionization (2) are given by

$$D_{J,l,j,J_f}=\hat{L}\hat{S}\hat{J}_f\hat{j}\begin{Bmatrix} L_f & l & L\\ S_f & \frac{1}{2} & S\\ J_f & j & J\end{Bmatrix}D_{J,l}, \tag{9}$$

where the matrix elements $D_{J,l}$ have a Fano-type energy dependence defined by

$$D_{J,d}=D^{\text{cont}}_{J,d}\left[\frac{V_{J,g}}{\sqrt{|V_{J,d}|^2+|V_{J,g}|^2}} - \frac{V^*_{J,d}}{\sqrt{|V_{J,d}|^2+|V_{J,g}|^2}}\,\frac{\epsilon_J+q_{J,d}}{\sqrt{\epsilon_J^2+1}}\right], \tag{10a}$$

$$D_{J,g}=D^{\text{cont}}_{J,g}\left[\frac{-V_{J,d}}{\sqrt{|V_{J,d}|^2+|V_{J,g}|^2}} - \frac{V^*_{J,g}}{\sqrt{|V_{J,d}|^2+|V_{J,g}|^2}}\,\frac{\epsilon_J+q_{J,g}}{\sqrt{\epsilon_J^2+1}}\right], \tag{10b}$$

with

$$\epsilon_J=\frac{E-E_J}{\Gamma_J/2}, \tag{10c}$$

$$q_{J,l}=\frac{V_{j,l}D^{\text{disc}}_J}{V_{j,l}D^{\text{cont}}_{J,l}}. \tag{10d}$$

Inserting those matrix elements into Eq. (13) of Ref. [12] the dynamic parameters $B_{k_0kk_\gamma}$ can be calculated.

In the determination of the relative strength of the different components of the $4f$ photoelectron multiplet only the ratio of the dipole transition-matrix elements $D_{J,g}/D_{J,d}$ and the ratio of the interaction matrix elements $V_{J,g}/V_{J,d}$ enter. Therefore the fine-structure patterns of the Eu $4f$ photoelectron spectra as a function of the photon energy can be predicted without knowing the absolute values of these matrix elements. For our calculations the ratio $D^{\text{cont}}_{J,g}/D^{\text{cont}}_{J,d}$ has been set equal to five based on Hartree-Fock calculations performed for photon energies well below the giant resonance. Ionization into the g continuum clearly prevails over ionization into the d continuum. A similar value is expected for the ratio $V_{J,g}/V_{J,d}$ of the interaction matrix elements. Autoionization into g-symmetric states is much more likely than autoionization into d-symmetric states. We estimated a value of 9.5 for this ratio [22].

Inspite of the considerable uncertainties of these ratios the fine-structure patterns of the $4f$ photoelectron spectra are expected to be described reasonably well by our model because these patterns are not very sensitive to the exact values of the above ratios as long as both values are well above unity.

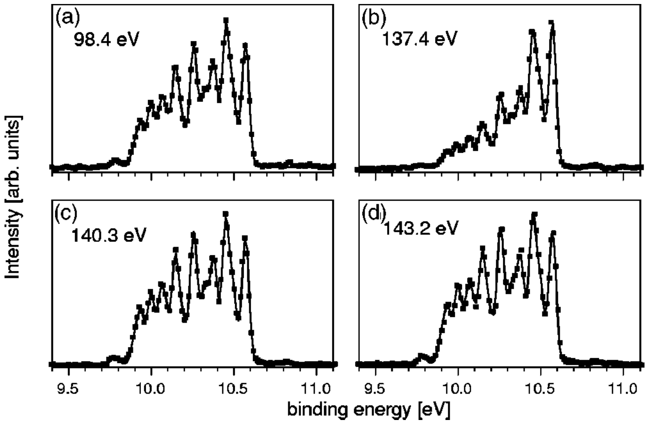

FIG. 3. Eu $4f$ photoelectron spectra for four different excitation energies. The solid lines are least-squares fits of 15 Gaussian profiles with equal widths and binding energies taken from Table I. The total resolution has been determined to 60 meV. The experimental uncertainties are smaller than the size of the symbols.

VI. UNPOLARIZED ATOMS

Figure 3 shows the Eu $4f$ photoelectron spectra taken at four different photon energies. For the spectrum in panel (a) a photon energy of 98.4 eV well below the giant resonance was chosen. The pattern of the photoelectron fine structure is very close to that obtained at photon energies near 50 eV (Fig. 1 and Ref. [7]). In panel (b) the photon energy was set to the low-energy rise of the resonance. Here the lines belonging to high total angular momenta are strongly enhanced in respect to the other lines. Panels (c) and (d) show spectra taken near the maximum and on the high-energy flank of the resonance. In both cases the shape of these spectra is again very similar to that outside the resonance.

This behavior can be explained using the *LS*-coupling model introduced in Sec. V. For photoelectron spectra of unpolarized atoms taken at the magic angle the sum in Eq. (1) reduces to only one term. The cross section is proportional to the parameter B_{000}. For this parameter Eq. (13) from Ref. [12] simplifies to

$$B_{000}=\sqrt{3}\hat{L}^2\hat{S}^2\hat{J}_f^2\sum_{lJ} C^0_{lJ}|D_{lJ}|^2\approx\sqrt{3}\hat{L}^2\hat{S}^2\hat{J}_f^2C^0_{gJ}|D_{gJ}|^2, \tag{11a}$$

with

$$C^0_{lJ}=\sum_x \hat{x}^2\begin{Bmatrix} S_f & L & x \\ l & J_f & L_f \end{Bmatrix}^2\begin{Bmatrix} S_f & L & x \\ J & \frac{1}{2} & S \end{Bmatrix}^2. \tag{11b}$$

In our case $|D_{dJ}|^2\leqslant\frac{1}{25}|D_{gJ}|^2$, and therefore has been neglected since only the squares of the matrix elements enter. The sum over the artificial quantum number x runs over all values allowed by the Wigner-6j symbols [9].

In panels (a)–(c) of Fig. 4 the relative intensities of the final-state fine-structure lines given by Eq. (11a) are plotted for each of the three possible intermediate states. In panel (d) the relative intensities of the final state are added under the assumption that each intermediate state is excited according to its multiplicity. This clearly is a good approximation for excitation energies far away from any resonances. The lines of panel (d) consequently show intensities proportional to the multiplicities of the final states. This is borne out by similarity of the patterns of panel (d) (Fig. 4) and the $4f$ photoelectron spectrum displayed in panel (a) of Fig. 3.

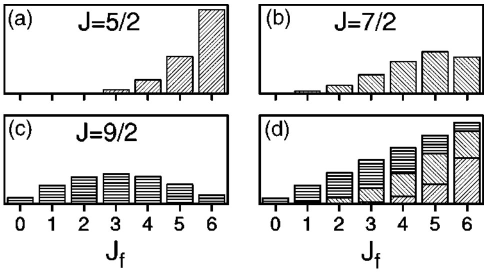

FIG. 4. Calculated Eu $4f$ photoelectron spectra for different final-state total angular momenta J_f of the remaining Eu$^+$ ion.

The calculated Eu $4f^7\,6s^2\;{}^7S_{7/2}\rightarrow 4f^6\,6s^2\epsilon l\;{}^8P_{5/2,7/2,9/2}$ partial cross sections are included in Fig. 2. As above only $|D_{gJ}|^2$ has been taken into account. The partial cross section of the ${}^8P_{5/2}$ final state is already enhanced close to the threshold of the giant resonance, while the partial cross sections for the ${}^8P_{7/2,9/2}$ channels are still very low. This explains the great similarity of the calculated fine-structure pattern in panel (a) of Fig. 4 with the experimental pattern shown in panel (b) of Fig. 3. Compared to the photoelectron spectrum taken below the resonance [panel (a) of Fig. 3] the lines corresponding to high values of the angular momentum of the remaining ion J_f are strongly enhanced. The experimental spectra taken at the peak of the giant resonance [panel (c) in Fig. 3] and several eV above the maximum [panel (d) in Fig. 3] are very similar to the spectrum taken outside the giant resonance [panel (a) in Fig. 3]. This is consistent with the predictions of our model because except for the region close to the threshold of the giant resonance the ratios of the partial cross sections of the ${}^8P_{5/2,7/2,9/2}$ channels are close to the statistical ratios outside the resonance.

In conclusion we can state that the *LS*-coupling model presented above yields a reasonable description of the changes of the characteristic pattern of the Eu $4f$ photoelectron spectra when tuning the photon energy through the giant resonance. Based on this we will use this model to describe the characteristic pattern of the LAD in the Eu $4f$ photoelectron spectra outside and in the giant resonance.

VII. LAD IN THE GIANT RESONANCE

In the photoionization of aligned atoms the photoemission cross section depends on the angle η between the linear polarization of the ionizing radiation and the alignment direction of the atoms. The difference between two photoelectron spectra taken for η and $\eta+90°$ is called the linear alignment dichroism (LAD$_\eta$). It depends on the factors B_{220}, B_{202}, B_{222}, and B_{242}. Since the LAD$_\eta$ changes harmonically with the angle η only two LADs are linearly independent. In this paper the LAD$_{0°}$ and the LAD$_{45°}$ are discussed. These LADs are defined by

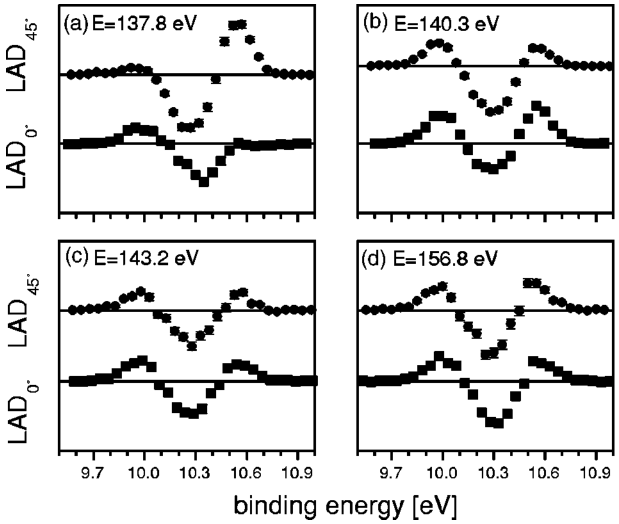

FIG. 5. Experimental LAD for four different excitation energies in the range of the giant resonance. The total resolution has been determined to 160 meV. The experimental uncertainties are given by error bars that are mostly smaller than the size of the symbols.

$$\mathrm{LAD}_{0^\circ} = I(\eta = 0^\circ) - I(\eta = 90^\circ), \tag{12a}$$

$$\mathrm{LAD}_{45^\circ} = I(\eta = 45^\circ) - I(\eta = -45^\circ). \tag{12b}$$

Inserting Eq. (1) into these equations and neglecting higher multipole moments than the quadrupole moment A_{20} for the ground state leads to

$$\mathrm{LAD}_{0^\circ} = K_{exp}\frac{\sigma}{4\pi}A_{20}(-0.33B_{220} - 1.37B_{202} + 0.55B_{222} + 1.27B_{242}), \tag{13a}$$

$$\mathrm{LAD}_{45^\circ} = K_{exp}\frac{\sigma}{4\pi}A_{20}(-0.91B_{220} - 0.76B_{222} - 0.57B_{242}). \tag{13b}$$

A. Fine-structure resolved LAD

Figure 5 shows both LAD patterns for four different photon energies in the region of the giant resonance. Panel (a) at the rising flank, panel (b) near the maximum and panels (c) and (d) on the high-energy slope of the resonance. At the highest photon energy (156.8 eV) shown in panel (d) the patterns of the LAD_{0° and the LAD_{45° are very similar. It has been shown that this pattern with two zero crossings and vanishing integral over the whole multiplet is typical for the LAD outside the resonance [9]. Experimentally this has been well established for the Eu $4f$ and Cr $3p$ photoelectron spectra [9].

A look on panels (a) and (b) of Fig. 5 reveals dramatic changes of the LAD patterns caused by the resonance. On the low-energy rise of the resonance [panel (a)] the LAD_{0° shows no positive lobe at the high binding-energy side while this lobe is clearly enhanced in the LAD_{45°. In the maximum of the resonance the same lobe is larger for the LAD_{0° than for the LAD_{45° [panel (b)]. The negative lobe of the LAD patterns is for both energies more pronounced in the LAD_{45°. At 143.2 eV [panel (c)] the LAD patterns have nearly reached their off-resonance shape.

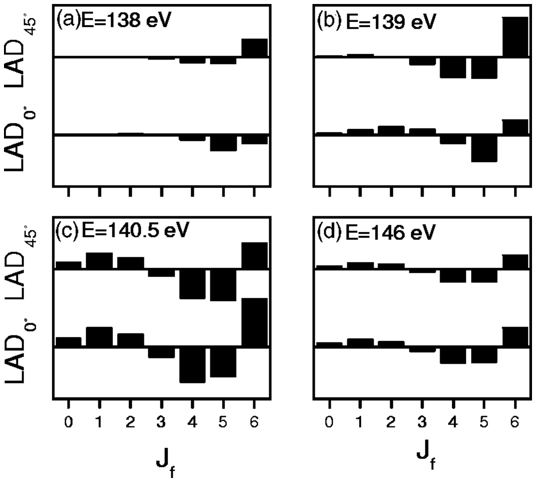

FIG. 6. LAD calculated with the *LS*-coupling model for four different energies within the range of the giant resonance.

These changes of the LAD patterns caused by the giant resonance can be explained qualitatively by our model. Figure 6 displays the patterns obtained by inserting the energy-dependent dynamic parameters $B_{k_0kk_\gamma}$ into Eqs. (13). Panels (a) and (b) of this figure correspond to photon energies in the rise of the resonance. A comparison of these panels shows that the LAD_{0° of the $J_f=6$ line changes its sign with increasing energy while the LAD_{45° of the same line remains positive. This explains the vanishing of the positive lobe for the LAD_{0° and its enhancement for the LAD_{45° in panel (a) of Fig. 5.

Panel (c) of Fig. 6 shows the calculated LAD patterns for excitation energies near the maximum of the resonance. They nicely reproduce the characteristic features of the experimental LAD patterns in panel (b) of Fig. 5, for example the enhanced positive lobe of the $J_f=6$ line for the LAD_{0°. Finally panel (d) of Fig. 6 verifies the close similarity of the two LAD patterns encountered for photon energies above the resonance [panel (d) of Fig. 5].

B. Fine-structure integrated LAD

For nonresonant excitation the positive and negative lobes of the LAD patterns cancel out exactly [9]. This sum rule leads to a complete disappearance of the dichroism if the fine structure in the photoelectron spectra is not experimentally resolved. In the case of resonant excitation this sum rule breaks down and dichroism can be observed in the total electron yield and in the absorption spectra.

Figure 7 shows the LADs obtained by integrating over the Eu $4f$ photoelectron multiplet taken at ten different energies inside and outside the giant resonance. Since each experimental data point of this figure is based on a complete dichroism measurement taking several hours, the factor K_{exp} in Eqs. (13) can vary strongly from point to point. To eliminate this problem the normalized linear alignment dichroism $\overline{(\mathrm{LAD})}$ defined by

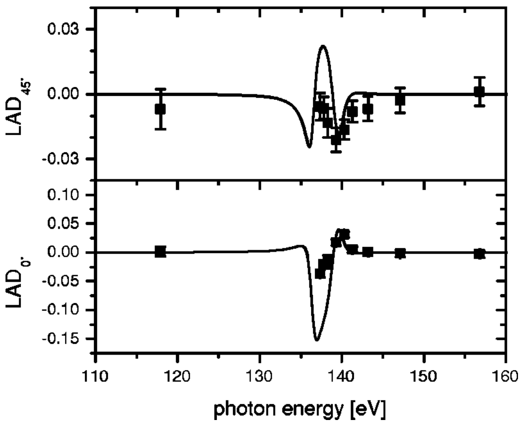

FIG. 7. Fine-structure integrated LADs for different excitation energies compared to the predictions of the *LS*-coupling model. For the $\mathrm{LAD}_{0°}$ the error bars are in the same order of magnitude as the symbols.

$$\mathrm{LAD}_{0°}=2\frac{I(\eta=0°)-I(\eta=90°)}{I(\eta=0°)+I(\eta=90°)}, \tag{14a}$$

$$\mathrm{LAD}_{45°}=2\frac{I(\eta=45°)-I(\eta=-45°)}{I(\eta=45°)+I(\eta=-45°)} \tag{14b}$$

is displayed in this figure. In agreement with the theoretical predictions the LAD vanishes outside the giant resonance, but there is a marked signal for the $\mathrm{LAD}_{45°}$ and the $\mathrm{LAD}_{0°}$ in the energy range of the resonance. The solid lines give the predictions of our model. The comparison of the calculated and experimental spectra demonstrates, that within the uncertainties, the model describes the characteristic features of the spectra reasonably well. Close to the maximum of the resonance, between 139 and 145 eV the data points follow the theoretical curve. The greatest deviations are encountered close to the minimum of the partial cross section at the threshold of the resonance. The small values for the denominator in Eqs. (14) result in considerable uncertainties.

It should be noted that the data in Fig. 7 still contain the angular resolution of the emitted electrons. To estimate the dichroism without angular resolution the factors $F_{k_0kk_\gamma}$ in Eq. (1) have to be integrated over the whole solid angle. For symmetry reasons these integrals vanish for all $F_{k_0kk_\gamma}$ with $k\neq 0$. In this case the $\mathrm{LAD}_{45°}$ vanishes and the $\mathrm{LAD}_{0°}$ is proportional to the dynamic parameter B_{202}. Since this parameter is the major contribution to the pattern of the $\mathrm{LAD}_{0°}$ in Fig. 7 the normalized linear dichroism in absorption spectroscopy should have a similar energy dependence.

VIII. LMDAD IN THE GIANT RESONANCE

The linear magnetic dichroism in the angular distribution (LMDAD) in the Eu 4f photoelectron spectra is given by the difference of the spectra of atoms laser oriented parallel and antiparallel to the propagation direction of the undulator radiation,

$$\mathrm{LMDAD}=I(\uparrow\uparrow)-I(\uparrow\downarrow). \tag{15}$$

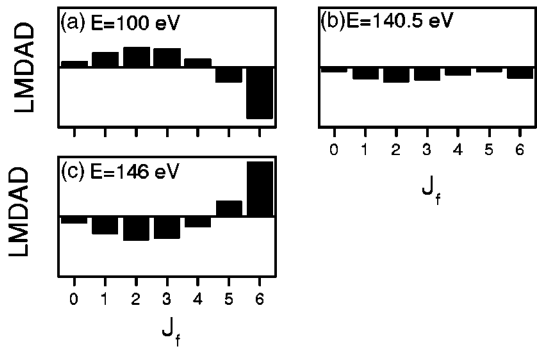

FIG. 8. Calculated LMDAD patterns for photon energies below, on, and above the giant resonance.

The orientation of the atoms is achieved by optical pumping using circularly polarized laser radiation. Taking only the first multipole moment, i.e., the orientation, of the atomic ensemble into account the LMDAD is given by

$$\mathrm{LMDAD}\propto A_{10}\sum_{\substack{ll'JJ'\\ J<J'}} C^{\mathrm{LMDAD}}_{ll'JJ'}(D_{lJ}D^{*}_{l'J'}-D^{*}_{lJ}D_{l'J'}). \tag{16}$$

The coefficients $C^{\mathrm{LMDAD}}_{ll'JJ'}$ can be calculated numerically. In contrast to the photoelectron spectra of unpolarized atoms and the LAD the complex dipole matrix elements enter, i.e., their absolute values and their relative phases. This renders the LMDAD a much more sensitive test of the theoretical approach. In our model the dipole matrix elements are given

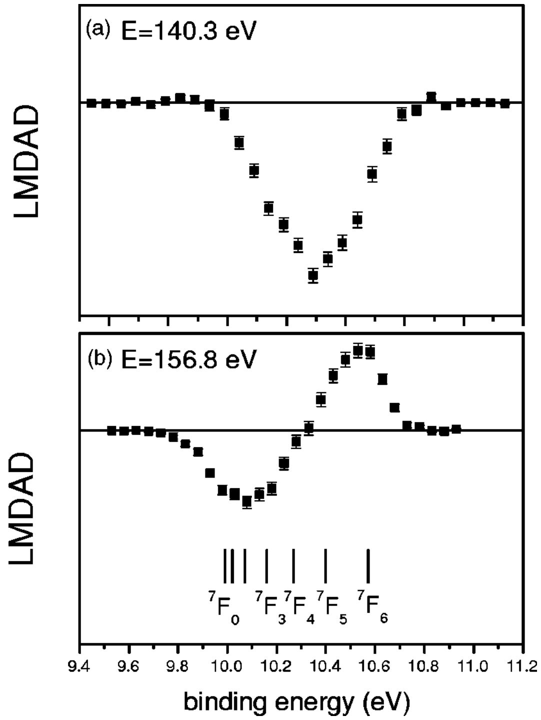

FIG. 9. Experimental LMDAD patterns for photon energies on and above the giant resonance. The total resolution has been determined to 160 meV.

by Eqs. (10). As above we assume that the dipole matrix elements $D_{J,d}^{\mathrm{cont}}$ and $D_{J,g}^{\mathrm{cont}}$ and the interaction matrix elements $V_{J,d}$ and $V_{J,g}$ are constant throughout the giant resonance. For the ratios $D_{J,g}^{\mathrm{cont}}/D_{J,d}^{\mathrm{cont}}$ and $V_{J,g}/V_{J,d}$ we assume the same values as above. By inserting the dipole matrix elements obtained from Eqs. (10) into Eq. (16) the LMDAD patterns displayed in Fig. 8 were calculated. For energies below the giant resonance [panel (a)] and for energies above the resonance [panel (c)] we get the same pattern except for a factor of (-1) which is caused by the phase change by π of the matrix element $D_{J,g}$ when tuning through the resonance. Both patterns show a positive and a negative lobe and a zero crossing in agreement with the predictions for the LMDAD patterns in nonresonant photoelectron spectra [9]. Near the maximum of the resonance [panel (b) of Fig. 8] the LMDAD deviates markedly from this pattern displaying only one broad negative lobe.

The experimental LMDAD patterns obtained on the maximum of the giant resonance and above the resonance are given in the upper and lower part of Fig. 9. Within the uncertainties there is a fair agreement between the experimental and theoretical patterns. The LMDAD for photon energies below the giant resonance [7] agrees well with the pattern calculated for a photon energy of 100 eV [23]. In the range of the onset of the resonance the calculated and experimental patterns differ considerably, but this is not a surprise since this range is very sensitive to the exact values of the parameters entering the model. Furthermore in this range, transitions to intermediate states that are not taken into account by the model contribute significantly.

IX. CONCLUSIONS

The linear dichroism in the Eu $4f$ photoelectron spectra excited within the giant $4d$-$4f$ resonance deviates markedly from the dichroism in the nonresonant spectra. The dramatic changes of the dichroism patterns when tuning the photon energy through the resonance are described qualitatively by a Fano-type model based on *LS* coupling. In agreement with the predictions of this model the dichroism in the resonance does not disappear, when the photoelectron spectra are integrated over all multiplet components. The corresponding sum rule for nonresonant photoemission breaks down within the resonance. For a quantitative description of the photoelectron spectra and the dichroism the model has to be extended in order to take the configuration interaction into account which clearly manifests itself in the high-resolution photoelectron spectrum.

ACKNOWLEDGMENTS

The authors want to thank the Deutsche Forschungsgemeinschaft for financial support and the HASYLAB staff for continuous assistance. Thanks are also due to M. Dickow and E. Heinecke for their help during the measurements.

---

[1] G. van der Laan, E. Arenholz, E. Navas, A. Bauer, and G. Kaindl, Phys. Rev. B **53**, R5998 (1996).

[2] G. van der Laan and B.T. Thole, Phys. Rev. B **48**, 210 (1993).

[3] H. Ogasawara, A. Kotani, and B.T. Thole, Phys. Rev. B **50**, 12 332 (1994).

[4] J. Morais, G.H. Fecher, R. Denecke, J. Liesegang, and C.S. Fadley, J. Electron Spectrosc. Relat. Phenom. **114-116**, 783 (2001).

[5] E. Arenholz, E. Navas, K. Starke, L. Baumgarten, and G. Kaindl, Phys. Rev. B **51**, 8211 (1995).

[6] W.J. Lademann, A.K. See, L.E. Klebanoff, and G. van der Laan, Phys. Rev. B **54**, 17 191 (1996).

[7] A. Verweyen, Ph. Wernet, B. Sonntag, K. Godehusen, and P. Zimmermann, J. Electron Spectrosc. Relat. Phenom. **101-103**, 179 (1999).

[8] J. Schulz, Ph. Wernet, K. Godehusen, R. Müller, P. Zimmermann, M. Martins, and B. Sonntag, J. Phys. B **35**, 907 (2002).

[9] A. Verweyen, A.N. Grum-Grzhimailo, and N.M. Kabachnik, Phys. Rev. A **60**, 2076 (1999).

[10] O. Zeybek, N.P. Tucker, S.D. Barrett, H.A. Dürr, and G. van der Laan, J. Magn. Magn. Mater. **196-197**, 740 (1999).

[11] U. Fano, Phys. Rev. **124**, 1866 (1961).

[12] S. Baier, A.N. Grum-Grzhimailo, and N.M. Kabachnik, J. Phys. B **27**, 3363 (1994).

[13] K. Starke, E. Navas, E. Arenholz, Z. Hu, L. Baumgarten, G. van der Laan, C.T. Chen, and G. Kaindl, Phys. Rev. B **55**, 2672 (1997).

[14] Ph. Wernet, J. Schulz, B. Sonntag, K. Godehusen, P. Zimmermann, A.N. Grum-Grzhimailo, N.M. Kabachnik, and M. Martins, Phys. Rev. A **64**, 042707 (2001).

[15] M. Martins, K. Godehusen, Ch. Gerth, P. Zimmermann, J. Schulz, Ph. Wernet, and B. Sonntag, Phys. Rev. A **65**, 030701(R) (2002).

[16] Ph. Wernet, A. Verweyen, J. Schulz, B. Sonntag, K. Godehusen, R. Müller, P. Zimmermann, and M. Martins, J. Phys. B **35**, 3887 (2002).

[17] A. Verweyen, Ph. Wernet, J. Schulz, B. Sonntag, M. Martins, K. Godehusen, and P. Zimmermann, J. Phys. B **32**, 4079 (1999).

[18] W. C. Martin, R. Zalubas, and L. Hagan, *Atomic Energy Levels – The Rare-Earth Elements* (University of California Press, Berkeley, 1978).

[19] M. Richter, M. Meyer, M. Pahler, T. Prescher, E.v. Raven, B. Sonntag, and H.-E. Wetzel, Phys. Rev. A **40**, 7007 (1989).

[20] A. Moewes, R.P. Winarski, D.L. Ederer, M.M. Grush, and T.A. Callcott, J. Electron Spectrosc. Relat. Phenom. **101-103**, 617 (1999).

[21] J. Schulz, dissertation, Universität Hamburg, 2001.

[22] The ratio $V_{J,g}/V_{J,d}$ has been obtained by trying several different values. While the influence of this ratio is negligible for the LAD the value 9.5 gives the best approximation for the measured LMDAD.

[23] The experimental geometry of Ref. [7] differs from the present geometry causing the LMDAD spectra to differ by a factor of (-1).

[24] N. M. Kabachnik and I. P. Sazhina, J. Phys. B **9**, 1681 (1976).